Proceedings of the Canadian Society for Mechanical Engineering International Congress
32nd Annual Conference of the Computational Fluid Dynamics Society of Canada
Canadian Society of Rheology Symposium
CSME-CFDSC-CSR 2025
May 25–28, 2025, Montréal, Québec, Canada

Large-eddy simulation of an offset jet flow over surface-mounted ribs

Mohammed Khalid Hossen, Ehsan Asgari, Mohammad Saeedi*, Baafour Nyantekyi-Kwakye
Department of Mechanical Engineering, Dalhousie University, Halifax, NS, Canada
*e-mail: mohammad.saeedi@dal.ca

Abstract- This article investigates the dynamics of turbulent structures in a three-dimensional offset jet flow over surface-mounted ribs using large-eddy simulations. The study aims to elucidate the effects of three ribs with different width-to-height ratios (e.g., W/H = 1, 2, and 3) on the flow field behavior in the wake region. A comprehensive analysis is then conducted to assess the flow characteristics across the three W/H ratios in recirculation, reattachment, redevelopment, and downstream regions. It is observed that flow separation occurs at the leading edge of the ribs and flow characteristics in the recirculation, reattachment, and redevelopment regions strongly depend on W/H ratios.

Keywords- Large-eddy simulation; offset jet; surface-mounted ribs.

I. INTRODUCTION

Turbulent jet flow is frequently encountered in various engineering applications, such as fluid injection systems, pollutant discharge, dam flow control, entrainment and mixing process in gas turbine and boiler combustion chambers and many others ([1], [2]).

Due to its relevance, numerous studies have been conducted to investigate the dynamics of coherent structures generated by submerged wall and offset jets. For instance, reference [3] and [4] both utilized PIV to investigate submerged three-dimensional turbulent offset jets discharged from round and rectangular nozzles, respectively. The study by reference [3] focused on how different exit Reynolds numbers (5000, 10000, and 20000) and offset heights (0, 0.5, 1.5, and 3.5) influence the jet flow characteristics. They observed that the associated recirculation region is strongly affected by the offset height ratio. The flow characteristics (e.g., decay and spread rates, profiles of mean velocities, reattachment length, turbulence intensities, and Reynolds shear stress) are nearly independent of Reynolds numbers. Similarly, reference [4] examined how various offset height ratios (0, 2, 4, and 8) impact the jet flow characteristics and evolution of coherent structures. Their study revealed that increasing the offset height ratio led to greater mean streamwise velocity decay rates, longer reattachment lengths, and larger coherent structures within the recirculation region.

Reference [5] conducted an experimental study to examine the flow behavior over surface-mounted transverse ribs with varying W/H ratios (1, 2, and 4) in a turbulent open channel flow. Their results showed that the reattachment length decreased as the W/H ratio increased, due to the development of secondary separation and reattachment on ribs with larger W/H ratios. Reference [6] experimentally investigated turbulent flow with varying streamwise W/H ratios (2, 2.5, 3, 4, 5, and 8) at a Reynolds number of 11,100. The study revealed that the flow behavior strongly depends on the ratios. For W/H = 1, the separated shear layer directly enters the wake, while for W/H = 2 and W/H = 2.5, it intermittently reattaches to the cylinder surface. For W/H $\geq$ 3, the shear layer fully reattaches to the cylinder, separates again from the trailing edge, and subsequently reattaches onto the bottom surface. Consequently, a large recirculation bubble forms in the wake for W/H = 1, but its size progressively decreases and stabilizes at a similar length for W/H $\geq$ 4.

Many numerical investigations are devoted to the study of the flow characteristics of either offset jet or surface-mounted rib flows in a turbulent regime. Please refer to [7], [8], [9], [10], and [11] for more details. Reference [12] conducted a numerical study on the interaction between a plane wall jet and a parallel offset jet using the finite volume method and large-eddy simulations (LES). Further, in the probability density function (PDF), they observed that the distribution of fluctuations near the jet exit is wide, but it gradually becomes narrower as the distance from the jet exit increases. One other work in this area is by [13], who experimentally investigated the interaction of surface-mounted square rib with a jet flow using PIV at a Reynolds number of 7600. In their study, the rib with W/H = 1 was positioned at three distinct locations downstream of the nozzle exit to analyze its effects on flow dynamics, including mean flow behavior and turbulence statistics.

To our knowledge, there have been no numerical investigations replicating the experimental study of offset flow over surface-mounted ribs described by [13], leaving many aspects of the underlying flow physics unexplored. This study uses LES to investigate the interaction between an offset jet and ribs with W/H = 1, 2, and 3, analyzing flow behavior, statistics, recirculation, shear layers, and dominant frequencies to reveal how rib geometry influences the flow dynamics. The simulations are performed in the same experimental domain as described in [13]. After validating the results through comparisons of the maximum of mean streamwise velocity, this study examines the effects of W/H ratios on first- and second-order statistics, as well as dominant flow frequencies for all ratios. The remainder of this paper is organized as follows below.

II. Test Case, Boundary Conditions, and Governing Equations

The test case is based on the PIV experiment conducted by [13]. Fig. 1 presents a schematic representation of the geometric configuration of the computational domain. The jet, with a rectangular cross-section, is positioned in the *y*-*z* plane, with a height h_J (≈ 0.008 m) and a width of $6h_J$. The inlet is offset by $2\,h_J$ from the bottom wall. The computational domain has dimensions $(L_x, L_y, L_z) = (28.75h_J, 14.5h_J, 25h_J)$. Figure 2 illustrates the mesh generation process, highlighting the slight variations in the total number of computational cells across the three cases. These differences arise from variations in rib geometry and mesh resolution, resulting in approximately 3 million cells for W/H = 1, 3.1 million for W/H = 2, and 3.17 million for W/H = 3.

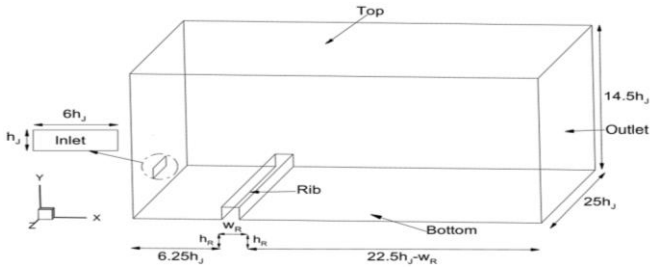

Fig. 1. Schematic representation of the computational domain.

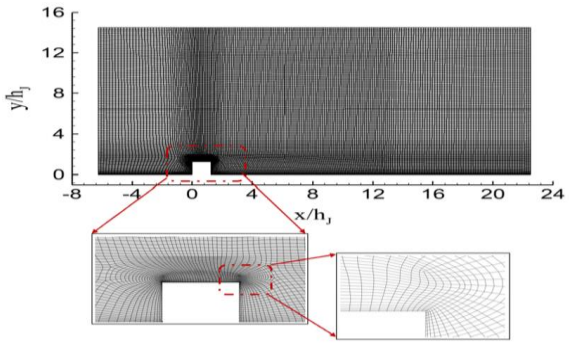

Fig. 2. Two-dimensional representation of the computational grid: the mid-span sideview (top), grid arrangement around the rib (bottom left), and near the rib corner (bottom right).

A parabolic velocity profile is implemented at the jet orifice (inlet) to mimic the uniform inlet condition as reported in the reference study [13] and is expressed as:

$$u(y) = \frac{3}{2} U_0 \left(1 - \left(\frac{y - \frac{h_J}{2}}{\frac{h_J}{2}}\right)^2\right), \tag{1}$$

where $u(y)$ is the velocity at a given point in the profile, and *y* is in the vertical direction. U_0 (0.95 m/s) is the reference velocity. A no-slip condition is applied on the left, bottom, and rib boundary surfaces, while a slip condition is applied on the front and back walls, and top surface. An outflow boundary condition ($\frac{\partial u}{\partial n} = \frac{\partial p}{\partial n} = 0$) is used in the outlet. A second-order central differencing scheme discretizes convection and diffusion terms, while a second-order implicit backward scheme handles time integration. The equations are solved in OpenFOAM using the PISO algorithm for pressure-velocity coupling. The time step is set to be 10^{-5} sec, keeping the maximum Courant-Friedrichs-Lewy (CFL) number below 0.2 throughout the simulations for numerical stability [11]. The flow-through time (FTT) of the simulation is 0.3 seconds. Convergence is monitored by ensuring that residuals drop below 10^{-6}, and statistics are collected over the final 5 FTTs after achieving a statistically steady state.

The filtered continuity and momentum equations for the LES of an incompressible fluid flow are provided as:

$$\frac{\partial \bar{u}_i}{\partial x_i} = 0, \tag{2}$$

$$\frac{\partial \bar{u}_i}{\partial t} + \bar{u}_j \frac{\partial \bar{u}_i}{\partial x_j} = -\frac{1}{\rho}\frac{\partial \bar{p}}{\partial x_i} + \nu \frac{\partial^2 \bar{u}_i}{\partial x_j \partial x_j} - \frac{\partial \tau_{ij}}{\partial x_j}, \tag{3}$$

where $\bar{u}_i$ represents the filtered velocity, $\bar{p}$ is the filtered pressure, and the term τ_{ij} is the so-called SGS stress tensor. The wall adaptive eddy viscosity (WALE) model for its ability to adapt to near-wall regions and capture small scale turbulence has been used to model the SGS stress tensor [14]. In the WALE model, the SGS viscosity is expressed as:

$$\nu_{sgs} = (C_w \Delta)^2 \frac{(S^d{}_{ij} S^d{}_{ij})^{\frac{3}{2}}}{(\bar{S}_{ij}\bar{S}_{ij})^{\frac{5}{2}} + (S^d{}_{ij} S^d{}_{ij})^{\frac{5}{4}}}, \tag{4}$$

where $\bar{S}_{ij}$ is the local strain tensor and the filter width is Δ. $S^d{}_{ij}$ is the traceless symmetric part of the velocity gradient tensor. The model coefficient was chosen as $C_w = 0.325$ [15].

III. Result Discussion

A. Validation

To validate the present simulation, the first- and second-order flow statistics are compared against the PIV measurement data for W/H = 1 [13]. Fig. 3a presents the streamwise evolution of the local maximum mean velocity normalized using the bulk inlet velocity. As is evident in the figure, a good agreement between the predicted evolution of W/H = 1 and the experimental measurement is observed. While both data sets generally follow a similar trend, a maximum relative error of approximately 9.1% between the measurement data and the predicted value is observed close to the jet inlet at $x/h_J = 2$. The discrepancies between the numerical and experimental data near the nozzle exit may be attributed to the vena contracta effect, which is not captured in the present simulation. For instance, Nyantekyi-Kwakye et al. (2015) observed that the maximum mean velocity of the jet increased with streamwise distance near the nozzle exit. The LES grid refinement study demonstrated that increasing the resolution had minimal impact, suggesting that the underprediction is due to the missing vena-contracta effect rather than insufficient grid resolution.

To further examine the effect of W/H ratios on the velocity decay, Fig. 3b shows the streamwise evolution of the

normalized maximum mean velocity for the three tested W/H ratios. The velocity distribution for the three W/H ratios follows a similar pattern. They gradually decrease as the flow develops downstream. As the W/H ratio increases, slight variations in the velocity distribution are observed. In the recirculation region at $x/h_J = 3$, a relatively rapid velocity decay is noted for W/H = 1, suggesting stronger turbulent mixing and more rapid energy dissipation. The ribs with W/H = 2 and W/H = 3, the velocity decay slows down, and the maximum velocity in the downstream region remains higher.

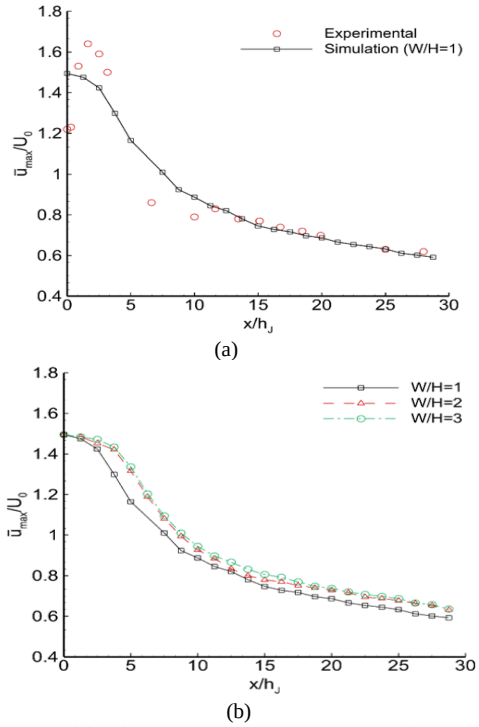

Fig. 3 Comparison of local maximum streamwise mean velocity decay: (a) between experimental data and W/H = 1, (b) among three different W/H ratios.

B. Flow Topology

Figure 4 shows the instantaneous streamwise velocity distribution around three ribs (W/H = 1, 2, and 3). A notable feature observed in these figures is the occurrence of flow separation followed by reattachment. The contours of the non-dimensionalized streamwise velocity ($\bar{u}/U_0$) clearly illustrate the jet reattaching to the channel bottom for all three W/H ratios. As the offset jet flow approaches the rib, it experiences an adverse pressure gradient that causes it to separate at the leading edge, forming a boundary layer. The separated shear layer leads to the formation of recirculation regions characterized by intense reverse streamwise velocities, observed both above for W/H = 3 and behind the ribs for all W/H ratios, consistent with the findings of [6]. The maximum reverse velocity within the recirculation region is approximately $0.1U_0$. The shear layer between the core jet and the slower recirculating flow induces intense reverse streamwise velocities. We can also observe that as the W/H ratio increases, there is an intensification of swirling motion and vortex formation [16], which will be discussed in later sections. They also illustrate how the jet spreads in the wall-normal direction in the wake.

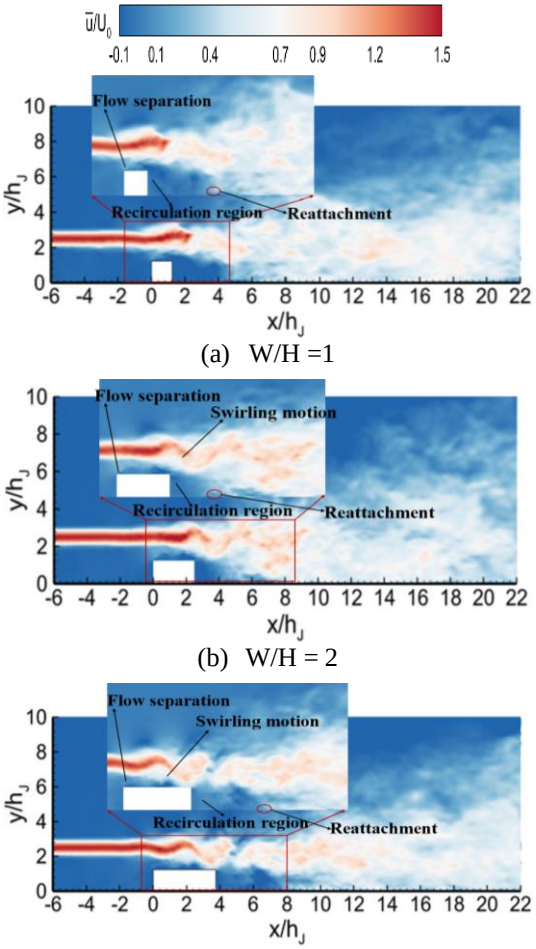

Fig. 4 Velocity contours of offset jet over surface-mounted ribs at the central plane ($z/h_J = 0$) for W/H = 1, 2, and 3.

Figure 5 shows a comparison of the mean streamwise velocity streamlines for all three W/H ratios. It can be observed that the offset jet flow separates and reattaches downstream of the ribs in all W/H ratios. The offset jet flow over rib of varying length produces up to two seperation regions. The evolution of these recirculation regions as a function of rib length. In Fig. 5a, the rib W/H = 1 show a single large recirculation region extending from the leading edge to the reattachment in the downstream surface. Additionally, in Fig. 5a, two small recirculation bubbles form above the rib surface, indicating the dividing streamlines substantially upward from the rib top surface. This phenomenon contributes to the increase in size and intensity of the separation bubble. In Fig. 5b, the rib with W/H = 2 shows the top and wake regions beginning to merge as they come closer together. Similarly, in Fig. 5c, the rib with W/H = 3 produces two recirculation regions: one at the top and another in the wake. In relative terms, the recirculation region for W/H = 1 is larger than those for W/H = 2, and 3. However, due to the additional recirculation region on top of the rib for W/H = 3, the recirculation region becomes larger than that for

W/H = 2. In this case, the mean velocity streamlines were used to estimate the size of the separation bubbles on top of the ribs as well as beyond the trailing edge. Recirculation length of 2.2, and 2.6 were recorded for W/H = 2, and W/H = 3, repectively on the top surface. The downstream recirculation lengths for W/H = 1, W/H = 2, and W/H = 3 were estimated to be 3.4, 2.8, and 3.3, respectively. Note that the downstream recirculation region is defined as the distance between the trailing edge and the reattachment point. The present observation corroborates results by [17] who investigated the turbulent flow dynamics over surface-mounted ribs with different W/H ratios (0.1 to 4).

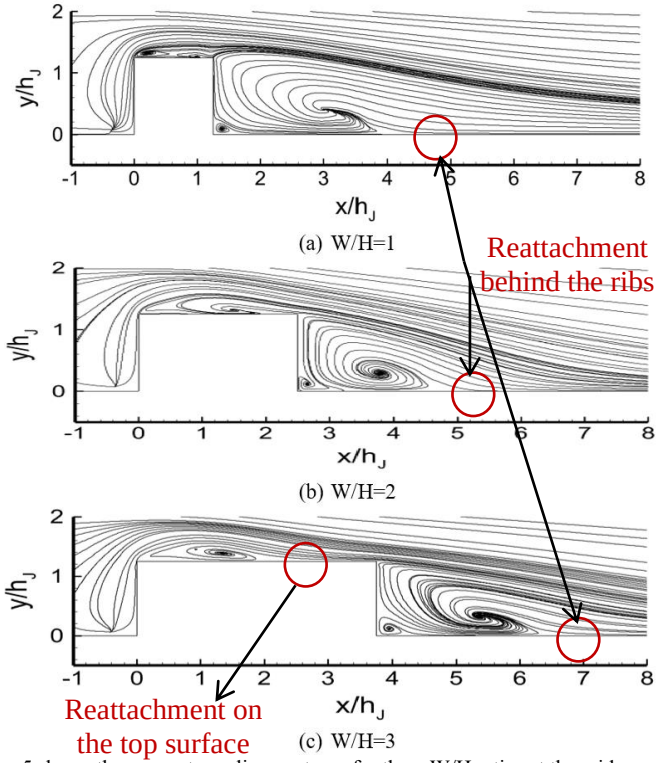

Fig. 5 shows the mean streamline contours for three W/H ratios at the mid-plane (z/h_J=0).

Figure 6 illustrates the eddy motion of an offset jet interacting with surface-mounted ribs of varying W/H ratios using a combination of Q-criterion and pressure fluctuations. The Q-criterion iso-surfaces, colored by the mean resolved velocity ($\bar{u}/U_0$), highlight large-scale coherent structures originating by the ribs and convected downstream, and also illustrating the interaction of vortices with regions of high and low velocity. On the other hand, instantaneous pressure fluctuations (p') are also analyzed to capture the dynamic effects of these vortical structures. Reference [18] investigated coherent structures in a wall jet flow using fluctuating pressure scaled with the maximum local velocity. Their results showed that pressure fluctuation contours mainly highlighted large-scale roll structures in the outer shear layer of the fully developed wall jet flow.

In Fig. 6, within a distance of $x/h_J \leq 5$ from the ribs, the vortices undergo significant stretching and interaction, eventually breaking into smaller-scale structures. Farther downstream, for $x/h_J > 8$, the flow transitions into a region dominated by large-scale rotation in the outer shear layer (e.g., red circular section). The pressure fluctuations plotted on the background plane reveal alternating regions of high and low pressure, coinciding with these large-scale vortices. These fluctuations are most intense near the ribs, and gradually diminish downstream, aligning with the development of the outer shear layer. For W/H = 2, and 3, the outer shear layer exhibits significant growth in both width and height after redevelopment of the flow.

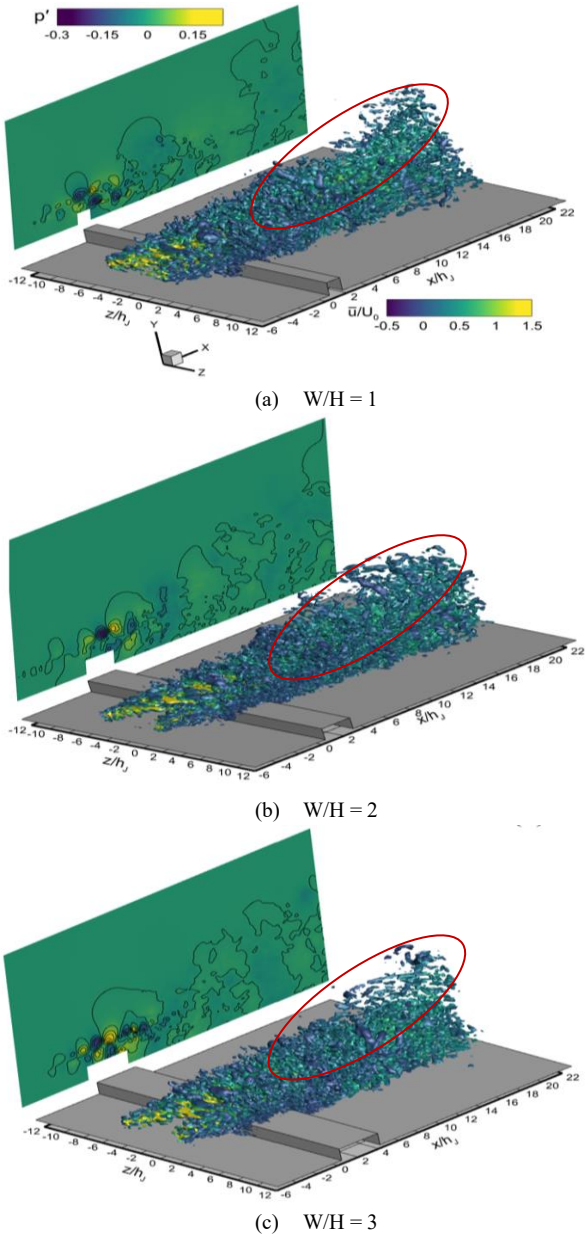

Fig.6 Iso-surface of second invariant of the velocity gradient tensor in the jet flow. The vertical plane (*x*-*y* plane) shows the contours of streamwise fluctuating pressure field at z/h_J = 0.

C. Turbulence Statistics

Figure 7 presents the vertical profiles of the mean streamwise velocity at two streamwise locations (m*, and e*). Here, m^* is the midpoint between the trailing edge and the recirculation reattachment point, and e^* is the reattachment point (see, Table 1 and Fig. 5).

Table 1 Approximate Streamwise locations of m^*, e^* for all W/H ratios.

	$m^*\,(x/h_J)$	$e^*\,(x/h_J)$
W/H = 1	3	4.6
W/H = 2	3.8	5.1
W/H = 3	5.2	6.8

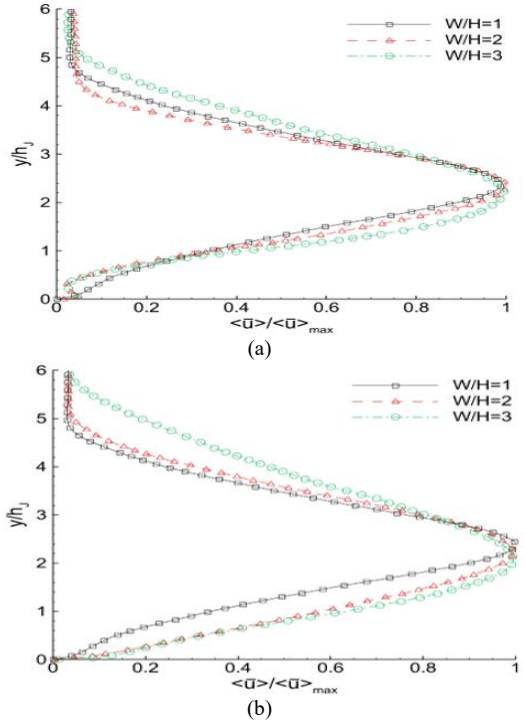

Fig. 7 Vertical profile of the normalized mean resolved streamwise velocity at (a) m*, and (b) e* in the center plane ($z/h_J = 0$).

The vertical profiles of streamwise mean velocity for all W/H ratios display central peaks downstream of the jet inlet, consistent with observations by [13]. The most noticeable differences in the velocity profiles among the three W/H ratios are observed in the regions $1 < y/h_J < 2.5$ and $3 < y/h_J < 5$ at m*, indicating that the mean velocity profile is significantly influenced by increasing W/H ratios. Fig. 7b shows the vertical velocity profile at e* for different W/H ratios. As W/H increases, the velocity profiles exhibit greater vertical entrainment of ambient fluid, indicating broader wakes at higher W/H ratios.

The joint probability density function (JPDF) is used to analyze how fluctuating velocities contribute to the Reynolds shear stress $\langle \bar{u}'\bar{v}' \rangle$. $\langle . \rangle$ represents time-averaged values. Following the quadrant analysis, the shear stress contributions are divided into four quadrants. The first quarnant Q1($\bar{u}' > 0, \bar{v}' > 0$) represents outward interaction. The second Q2 ($\bar{u}' < 0, \bar{v}' > 0$) corresponds to ejection events, the third Q3($\bar{u}' < 0, \bar{v}' < 0$) indicates inward interaction, and the fourth quadrant Q4($\bar{u}' > 0,\ \bar{v}' < 0$) relates to sweep events [6], [12]. Fig. 8 presents the JPDF of streamwise and vertical velocity fluctuations for all ribs. The JPDF contours are computed at downstream location ($x/h_J = 4$). The x-axis shows σ_u (or $\bar{u}'/\bar{u}'_{rms}$) and the y-axis shows σ_v (or $\bar{v}'/\bar{v}'_{rms}$), which are normalized by their respective RMS values. In these figures, Q2 and Q4 events (e.g., $-\langle \bar{u}'\bar{v}' \rangle$) are the predominant features in the shear layer across all W/H ratios. The JPDF shows a strong skewness towards Q2-Q4 events, highlighting the dominance of low-momentum fluid ejections away from the shear layer Q2 and high-momentum fluid sweeps into the shear layer Q4. This increased probability for W/H = 3 is primarily attributed to the turbulent wakes generated by the ribs. On the other hand, the probabilities of mean shear stress associated with Q1 (outward) and Q3 (inward) remain nearly equal for W/H = 1, 2, and 3.

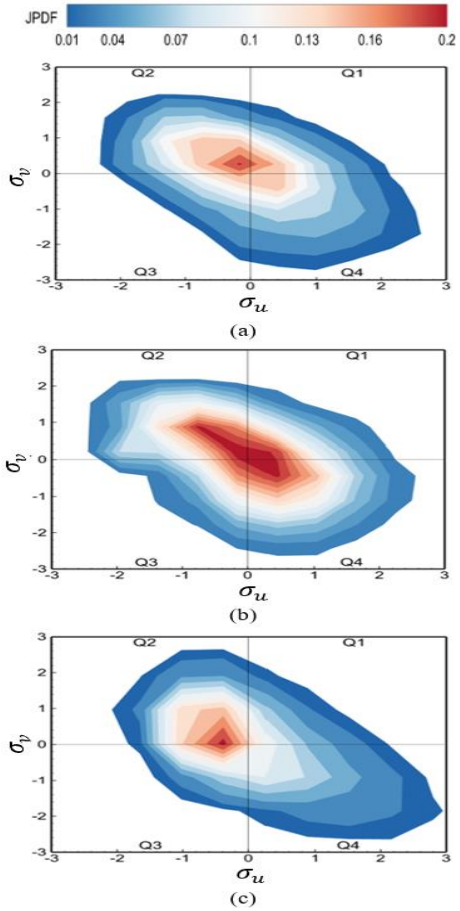

Fig: 8 JPDF of streamwise instantaneous fluctuation velocity in downstream locations at $x/h_J = m$*, for $y/h_J =$ 1.5 and $z/h_J =$ 0.

D. Spectral Analysis

Figures 9a and 9b show the PSD of the instantaneous streamwise and vertical resolved fluctuating velocity for all W/H ratios at $x/h_J = m$*. In these figures, the frequency is normalized by the Strouhal number, defined as $St = fL/U_0$, where f is the frequency, L is the characteristic length scale.

Figure 9a shows the PSD for W/H = 1, 2, and 3, with distinct peaks at different frequencies. For W/H = 1, the largest peak appears at St = 2 (black dashed line). For W/H = 2, the peak occurs at St = 2.3 (red dashed line), while for W/H = 3, the peak is near St = 8 (green dashed line). In Fig. 9b, the case of W/H = 1 shows the highest peak occurring at St = 4. For W/H = 2, multiple peaks are observed with the largest peak at St = 8. Similarly, for W/H = 3, the main peak also occurs near St = 8. Overall, on Fig. 9, the dominant peaks at low frequencies for all W/H ratios indicate vortex shedding driven by large-scale structures and intermittent interactions between large and small scales. While the inertial subrange shows energy transfer across frequencies and follows a slope of -5/3 [9].

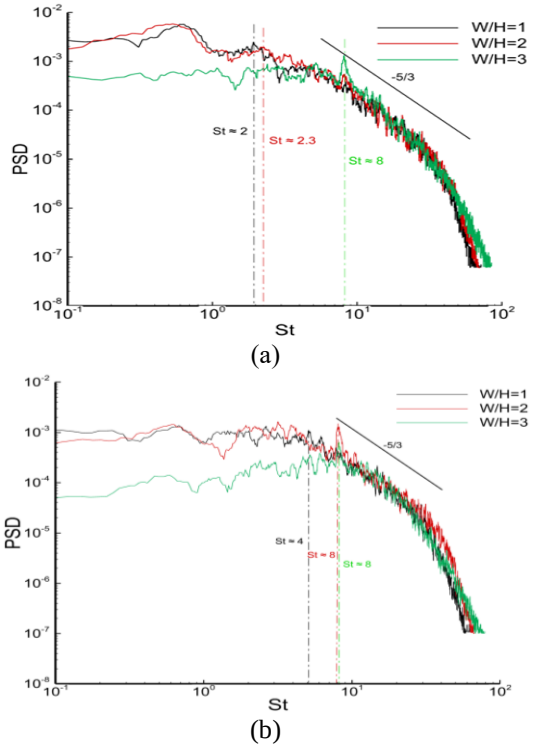

Fig. 9 Power spectral density of (a) streamwise and (b) vertical fluctuations velocity at $x/h_J = m^*$, for $y/h_J =$ 1.5 and $z/h_J =$ 0.

IV. CONCLUSION

The effects of W/H = 1, 2, and 3 on flow characteristics were analyzed using the LES. This study focuses on understanding the flow topology, coherent structures, and turbulence characteristics in the recirculation region, at the reattachment point, and in downstream locations. It is observed that the predicted results agree well with the reference data for the normalized local maximum resolved velocity. As the W/H ratio increases, the shear flow splits twice: first at the reattachment point on top and then behind the obstacle. The recirculation region behind the W/H ratios becomes smaller with increasing W/H. However, for rib with W/H = 3, the recirculation region remains larger due to reattachment on top of the ribs. For JPDF, ejections and sweeps dominate outward and inward interactions across all W/H ratios behind the ribs. Spectral analysis reveals dominant low-frequency peaks associated with large-scale vortex shedding in the wake regions.

ACKNOWLEDGMENT

The authors acknowledge financial support from the Faculty of Engineering, Dalhousie University. The support of the Supercomputing Facility by the Digital Research Alliance of Canada is also gratefully acknowledged.

REFERENCES

[1] Assoudi, A., Habli, S., Saïd, N. M., Bournot, H., & Le Palec, G. (2015). Experimental and numerical study of an offset jet with different velocity and offset ratios. Engineering Applications of Computational Fluid Mechanics, 9(1), 490–512.

[2] Kumar, A. (2015). Mean flow characteristics of a turbulent dual jet consisting of a plane wall jet and a parallel offset jet. Computers & Fluids, 114, 48–65.

[3] Agelin-Chaab, M., & Tachie, M. F. (2011). Characteristics and structure of turbulent 3D offset jets. International Journal of Heat and Fluid Flow, 32(3), 608–620.

[4] Nyantekyi-Kwakye, B., Tachie, M. F., Clark, S. P., Malenchak, J., & Muluye, G. Y. (2015). Experimental study of the flow structures of 3D turbulent offset jets. Journal of Hydraulic Research, 53(6), 773–786.

[5] Atamanchuk, K. M., & Tachie, M. F. (2014). PIV Investigation of Separated and Reattached Turbulent Flows Over Ribs of Various Aspect Ratio. Fluids Engineering Division Summer Meeting, 46247, V01DT27A010.

[6] Agyei-Agyemang, K. H., Essel, E. E., & Tachie, M. F. (2023). Effects of Aspect Ratio on Flow Characteristics on Free Surface-mounted Rectangular Cylinders. ICHMT DIGITAL LIBRARY ONLINE.

[7] Pramanik, S., & Das, M. K. (2013). Numerical characterization of a planar turbulent offset jet over an oblique wall. Computers & Fluids, 77, 36–55.

[8] Saeedi, M., LePoudre, P. P., & Wang, B.-C. (2014). Direct numerical simulation of turbulent wake behind a surface-mounted square cylinder. Journal of Fluids and Structures, 51, 20–39.

[9] Saeedi, M., & Wang, B.-C. (2015). Large-eddy simulation of turbulent flow and dispersion over a matrix of wall-mounted cubes. Physics of Fluids, 27(11).

[10] Ma, R., Alamé, K., & Mahesh, K. (2021). Direct numerical simulation of turbulent channel flow over random rough surfaces. Journal of Fluid Mechanics, 908, A40.

[11] Asgari, E., & Saeedi, M. (2024). Direct numerical simulation of laminar boundary layer interaction with a wall-mounted circular cylinder at low-Reynolds number. Physics of Fluids, 36(8).

[12] Li, Z. W., Huai, W. X., & Han, J. (2011). Large Eddy Simulation of the interaction between wall jet and offset jet. Journal of Hydrodynamics, 23(5), 544–553. https://doi.org/10.1016/S1001-6058(10)60148-5.

[13] Nyantekyi-Kwakye, B., Tachie, M. F., & Clark, S. P. (2016). Flow characteristics of an offset jet over a surface mounted square rib. Journal of Turbulence, 17(8), 727–757. https://doi.org/10.1080/14685248.2016.1174779.

[14] Nicoud, F., & Ducros, F. (1999). Subgrid-scale stress modelling based on the square of the velocity gradient tensor. Flow, Turbulence and Combustion, 62(3), 183–200.

[15] Shukla, A. K., Dewan, A., Singh, D. K., & Singh, T. P. (2023b). Heat transfer characteristics of jet impingement on a surface mounted with ribs using LES. International Journal of Thermal Sciences, 187, 108210.

[16] Chalmers, H., Fang, X., & Tachie, M. F. (2021). Streamwise Aspect Ratio Effects on Turbulent Flow Separations Induced by Forward-Backward-Facing Steps. Journal of Fluids Engineering, Transactions of the ASME, 143(2). https://doi.org/10.1115/1.4048686

[17] Hwang, R. R., Chow, Y. C., & Chiang, T. P. (1999). Numerical predictions of turbulent flow over a surface-mounted rib. Journal of Engineering Mechanics, 125(5), 497–503.

[18] Banyassady, R., & Piomelli, U. (2014). Turbulent plane wall jets over smooth and rough surfaces. Journal of Turbulence, 15(3), 186–207.